ADVANCING EARTH AND SPACE SCIENCES

Geochemistry, Geophysics, Geosystems

RESEARCH ARTICLE
10.1029/2023GC011431

Key Points:
- Mantle-derived intrusion has been detected in the crust beneath the Qujiang fault (QJF) and Shiping-Jianshui fault (SJF)
- Tectonics remains active at the front edge of the Sichuan-Yunnan block, and stresses accumulate on the QJF and SJF
- The current movement of the Xiaojiang fault may not cut through the Red River fault and continue southward

Supporting Information:
Supporting Information may be found in the online version of this article.

Correspondence to:
Y. Li,
liying@ief.ac.cn

Citation:
Shao, W., Liu, Z., Li, Y., Chen, Z., Lu, C., Zhao, C., et al. (2024). Geochemical characteristics of thermal springs and insights into the intersection between the Xiaojiang fault and the Red River fault, southeastern Tibet Plateau. *Geochemistry, Geophysics, Geosystems*, *25*, e2023GC011431. https://doi.org/10.1029/2023GC011431

Received 5 JAN 2024
Accepted 5 FEB 2024

Author Contributions:
Conceptualization: Weiye Shao, Ying Li, Zhi Chen
Data curation: Weiye Shao, Yun Wang
Formal analysis: Weiye Shao, Ciping Zhao, Qilin Li, Shaohui Fan
Funding acquisition: Weiye Shao, Ying Li, Ciping Zhao, Yun Wang
Investigation: Weiye Shao, Yun Wang, Hua Ran
Methodology: Weiye Shao, Ciping Zhao, Qilin Li
Supervision: Ying Li, Zhi Chen

Geochemical Characteristics of Thermal Springs and Insights Into the Intersection Between the Xiaojiang Fault and the Red River Fault, Southeastern Tibet Plateau

Weiye Shao[1,2], Zhaofei Liu[3], Ying Li[1], Zhi Chen[1], Chang Lu[1], Ciping Zhao[2], Yun Wang[4], Qilin Li[2], Zihan Gao[1], Yili Luo[1], Hua Ran[2], and Shaohui Fan[2]

[1]CEA Key Laboratory of Earthquake Prediction, Institute of Earthquake Forecasting, Beijing, China, [2]Yunnan Earthquake Agency, Kunming, China, [3]School of the Earth and Resources, China University of Geosciences, Beijing, China, [4]Department of Insurance, School of Finance, Yunnan University of Finance and Economics, Kunming, China

Abstract During the ongoing uplift and expansion of the southeastern margin of the Tibetan Plateau, the front edge of the Sichuan-Yunnan rhombic block (SYB) has experienced intense tectonic activity and frequent seismicity. In this study, the fluid geochemistry in the primary active faults at the front edge of the SYB was investigated, with the aim of understanding the tectonic activity and intersection relationship between the Xiaojiang fault (XJF) and the Red River fault (RRF). Thermal spring water and gases exhibit a coupled spatial distribution relationship; relatively high ion concentrations and $^3He/^4He$ ratios (Rc/Ra ratios of 0.21 to 0.62Ra) are observed along the RRF, Qujiang fault (QJF), and Shiping-Jianshui fault (SJF). Multidisciplinary research results have indicated that mantle-derived intrusion has been detected in the crust beneath the QJF and SJF. The current tectonic activity in the front edge of the SYB remains intense, with compressive stresses shifting toward the western side of the XJF and accumulating on the QJF and SJF. This has led to the development of fractures, enhancing the water–rock interaction and deep-derived gas degassing along the faults. The unmixing characteristics of fluids at the intersection area of these two faults suggest the absence of conduits for fluid migration between the faults. Owing to the lower gas $^3He/^4He$ ratios, lower shear strain rates, stable reservoir temperature field, and extremely low historical seismicity in the Indo-Chinese block, it is speculated that the current movement of the XJF may not cut through the RRF and continue southward.

Plain Language Summary Fluids serve as carriers of information regarding deep activities, and are known to migrate along active faults. Additionally, fluid geochemistry is highly sensitive to tectonic activity. Given the intense tectonic activity and frequent seismicity experienced at the front edge of the Sichuan-Yunnan rhombic block (SYB), our study focuses on investigating the fluid geochemical characteristics of the primary active faults in this region. Significant spatial differences in fluid chemistry are observed, particularly with respect to relatively high ion concentrations and mantle He values along the Red River fault (RRF), Qujiang fault (QJF), and Shiping-Jianshui fault (SJF). Furthermore, the lack of conduits facilitating fluid migration between the Xiaojiang (XJF) and RRF is evident from the distinct unmixed characteristics of the fluids. Multidisciplinary results indicate the presence of mantle-derived intrusion into the crust beneath the QJF and SJF. The compressive stresses have shifted toward the western side of the XJF and are accumulated on the QJF and SJF, resulting in the observed spatial variations in fluid geochemistry. Ultimately, these spatial differences can be attributed to the unique intersection relationship between the XJF and RRF.

1. Introduction

Fluids are crucial carriers that exchange matter and transfer energy, reflecting unique geological, geochemical, and hydrological information (Caracausi & Sulli, 2019; Kulongoski et al., 2013; Skelton et al., 2014). Due to their ease of migration, fluids circulate through tectonic discontinuities, such as active faults or high-permeability cracks, until they are discharged to the surface (Faulkner et al., 2010; Gori & Barberio, 2022; Y. Li et al., 2013). The presence of mantle-derived volatiles in fluids, such as ^3He and CO_2, provides direct evidence of the connection between the fault and the deep mantle (Z. Chen et al., 2020; McGibbon et al., 2018; M. Zhang et al., 2021). Particularly for strike-slip fault zones with large cutting depths, strong seismic activity, and high permeability, mantle-derived volatiles exhibit rapid migration. For example, high contributions of mantle-derived gas components have been observed in the Xianshuihe Fault in China (W. Liu et al., 2023; Tian et al., 2021), the North Anatolian Fault in Turkey (Doğan et al., 2009), and the San Andreas Fault in the United States (Kulongoski

Visualization: Weiye Shao, Zhaofei Liu, Zihan Gao
Writing – original draft: Weiye Shao
Writing – review & editing: Weiye Shao, Zhaofei Liu, Ying Li, Zhi Chen, Chang Lu, Ciping Zhao, Yili Luo

et al., 2013; Yasin & Yüce, 2023). These deep fluids provide crucial information for understanding material cycling and geodynamic processes along fault zones and for revealing stress accumulation and seismic activity (Y. Li et al., 2023; Sano et al., 2014). Additionally, fluids are highly sensitive to changes in porosity. In tectonic zones with seismic activity, stress accumulation, and active faulting - especially at the fault intersection - when the degree of fracture development changes, the physical and chemical parameters of fluid can change quickly (Hosono et al., 2020; Italiano et al., 2014; Moore et al., 2009; Ring et al., 2016). Fluids with different compositions can mix depending on the connectivity of the fault (Gómez Díaz & Mariño Arias, 2020; Shoedarto et al., 2021; Williams et al., 2013). Therefore, thermal springs along fault zones have become one of the most direct objects for studying the characteristics of fault activity, fault connectivity, and changes in the stress state.

As a result of the India-Asia continental collision, the southeastern margin of the Tibet Plateau is one of the most active tectonic deformation regions, with the occurrence of large-scale plateau uplift, intracontinental deformation, and material escaping clockwise around the eastern Himalayan syntaxis (Shi & Wang, 2017; Tapponnier et al., 1982; Z. Xu et al., 2016). The Xiaojiang fault (XJF) and the Red River fault (RRF) are strike-slip boundary faults that play a significant role in the tectonic evolution and material escape process on the southeastern margin of the Tibetan Plateau, forming the southeastern and southwestern boundaries of the Sichuan-Yunnan rhombic block (SYB), respectively (Xiang et al., 2000). The intersection area of the two faults is the forefront area of the rotation and extrusion of the SYB (Tong et al., 2015), where subordinate faults are developed and earthquakes occur frequently. Therefore, the front edge of the SYB is an active tectonic area.

During uplift and deformation in the southeastern margin of the Tibetan Plateau, the tectonic evolution, crustal deformation, and seismic activity of the front edge of the SYB provide crucial constraints on various kinematic models (Bao et al., 2015; Bischoff & Flesch, 2018; Flesch et al., 2001; Leloup et al., 1995). The intersection relationship between the XJF and RRF is a fundamental issue when studying the deformation characteristics of the front edge of the SYB. Thus, a crucial research area is whether the XJF crosscuts through the RRF and moves southward, which would affect the current tectonic pattern and stress distribution in the southeastern margin of the Tibetan Plateau (Y. Li et al., 2019; Z. Li et al., 2020; Michel et al., 2000; Schoenbohm et al., 2006; Z. Shen et al., 2005; Y. Wang, Zhang, et al., 2014). The frequent occurrence of strong earthquakes along the eastern boundary of the SYB has intensified the rotation of the block with ongoing southward compression, making it necessary to further investigate the tectonic activity of the front edge of the SYB. Some studies on geothermal fluid geochemistry in the area have focused on the hydrothermal circulation characteristics and volatile origin at both a single fault and limited locations at the front edge of the SYB (He et al., 2023; C. Li et al., 2021; Shao et al., 2022; Y. Wang, Zhao, et al., 2014; X. Zhou et al., 2020). Nevertheless, fluid geochemistry research on the intersection relationship between the XJF and RRF is lacking, and the relationship between fluid geochemistry and regional tectonic features in the front edge of SYB remains unclear.

In this study, the spatial distribution of fluid geochemistry, mixing and circulation evolution characteristics, and the origin of deep fluids in and around the front edge of the SYB are investigated. Fluid geochemistry and geophysics are used in conjunction to determine the relationship between current tectonic activities and fluid geochemistry, revealing the current tectonic stress state.

2. Geological Setting

During the northward subduction of the Indian plate, a series of large-scale NNW-SN strike-slip fault systems developed on the southeastern edge of the Tibet Plateau (Yin & Harrison, 2000). The plateau is divided by these complex large-scale strike-slip faults, giving rise to intracontinental microplates, with the SYB being one of the most active blocks (Figure 1). The XJF, a near N-S spreading strike-slip fault, serves as the eastern boundary fault of the SYB. It extends for about 400 km, ranging from the Qiaojia Basin in the north to the RRF in the south. It can be divided into three sections: the northern section consists of a single fault, the middle section of Dongchuan-Huaning is divided into two east and west branches separated by a distance of ∼15 km, and the southern section is further divided into multiple branches. Based on GPS observation data, the strike-slip rate of the northern and middle sections of the XJF is estimated to be 8–11 mm/a (Wen et al., 2011; G. Zheng et al., 2017). For the southern section, some researchers have calculated a slip rate of 7–9 mm/a (Q. Li et al., 2019; Z. Li et al., 2019; Z. Shen et al., 2005), which is not limited by the RRF. Wen et al. (2011), Y. Wang, Zhang, et al. (2014) have suggested that, after passing through Tonghai and Jianshui, the sliding rate of the southern section of the XJF decreases to ∼4 mm/a. This rate reduction is attributed to the adjustment of strike-slip and shortening deformation

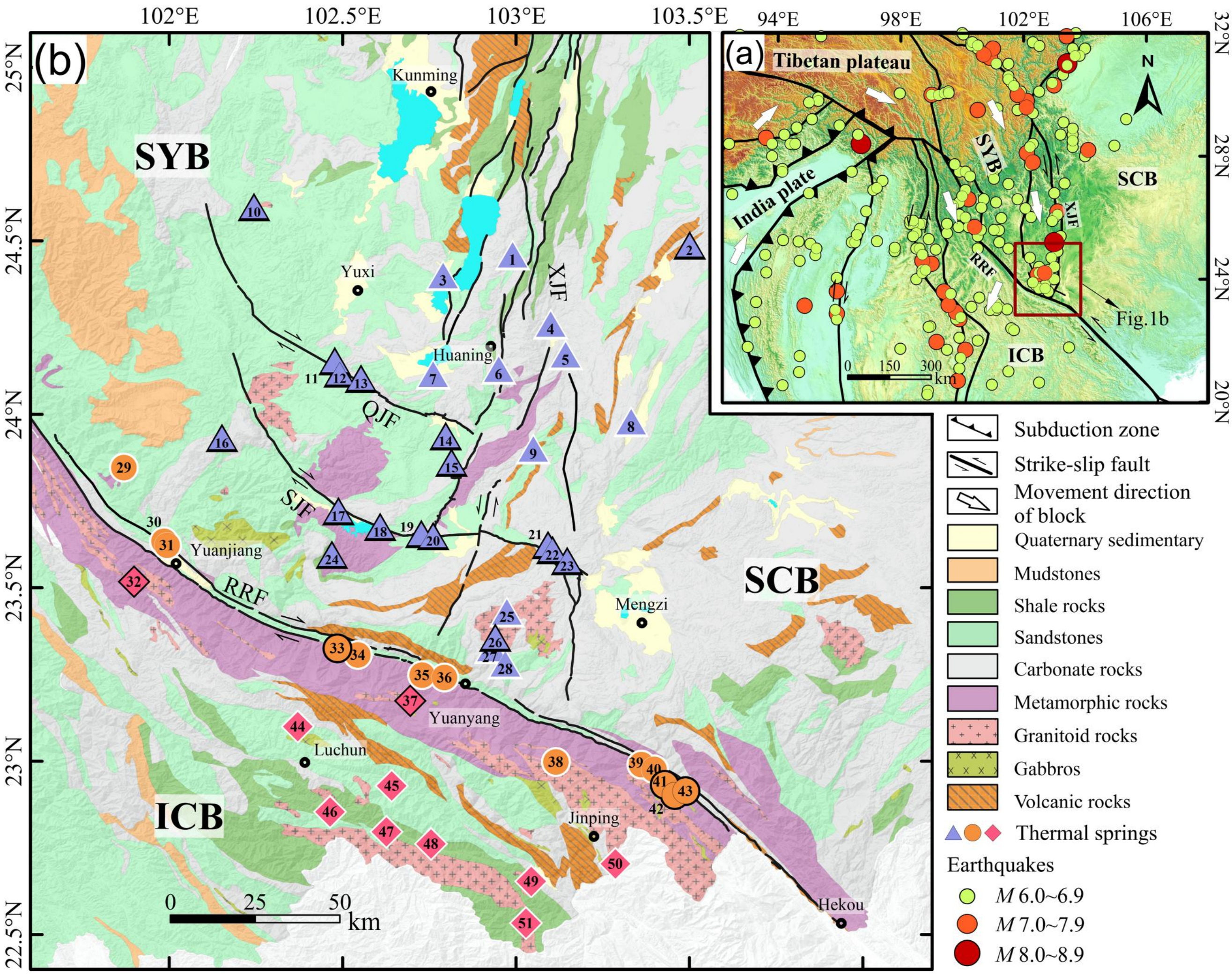

Figure 1. (a) Simplified tectonic map of the southeastern Tibetan Plateau and adjacent regions. The Xiaojiang fault (XJF) and the Red River fault (RRF) are boundary faults between the Sichuan-Yunnan block (SYB), Indo-China block (ICB), and South China block. Large earthquakes ($M \geq 6.0$) have occurred since 1900, data for which are obtained from the National Earthquakes Data Center (https://data.earthquake.cn/). The red box indicates the location of the study area. (b) Map showing regional geology (modified from Ma et al. (2002)), fault distribution (quoted from Q. Deng et al. (2003)), and thermal spring sampling sites in the study area. QJF: Qujiang fault; SJF: Shiping-Jianshui fault. Numbered triangles, circles, and diamonds represent sampling sites along or near the XJF (including Qujiang fault and SJF) and RRF, and within the ICB, respectively. The black and white borders of the numbered points represent the sampling points in this study and the ones from previous studies (C. Li et al., 2021; Z. Li et al., 2022; L. Shen et al., 2007; Y. Wang, 2021; Y. Wang et al., 2020; K. Zhao et al., 2005; X. Zhou et al., 2020), respectively.

along subordinate faults, such as the Qujiang fault (QJF) and Shiping-Jianshui fault (SJF) at the front edge of the SYB. In addition, Z. Li et al. (2020) believe that the southern segment of the XJF undergoes diffuse deformation. In terms of the fault spatial distribution, some researchers have suggested-through geological studies-that the southern section of the XJF is less active, with a strike-slip rate of 1.66 mm/a and does not intersect (He et al., 1993; Song et al., 1998) or cut through the RRF (Schoenbohm et al., 2006). However, Han et al. (2017) argue that the XJF cuts through the RRF to the south, which is supported by the tectonic models proposed by E. Wang et al. (1998), Michel et al. (2000), and Z. Wu et al. (2015). Furthermore, seismological results (Dong et al., 2023) reveal that the southern segment of the XJF is unaffected by the RRF and cuts through the RRF to the south. Geomagnetic results (Ye et al., 2022) suggest that the XJF may not develop southward beyond the RRF. There are certain discrepancies in the findings regarding the intersection relationship between the XJF and the RRF, which is a fundamental issue that must be resolved in the study area.

The RRF is the northeastern boundary of the Indo-Chinese block (ICB) and the southwestern boundary of the SYB, with a distinct arcuate division in the geomorphology (Replumaz et al., 2001; Schoenbohm et al., 2006); the arcuate curvature is believed to result from the rotational extrusion of the SYB (Allen et al., 1984; E. Wang et al., 1998; Wen et al., 2022). The RRF is divided into three segments in China. The southern section of the RRF, Yuanjiang-Hekou, in the present study, has a rightward slip rate of 0.9–1.4 mm/a and ∼1.6 mm/a reverse strike due to SYB extrusion (Z. Li et al., 2020; Pan & Shen, 2017).

The XJF, as a section of the North-south Seismic Belt in China, has historically experienced a number of large earthquakes above *M*7.0, such as the Songming *M*8.0 earthquake in 1833 and the Huaning *M*7.0 earthquake in 1789 (Wen et al., 2008). Over the last 400 years, no earthquakes *M*7.0 or above have occurred in the southern section of the XJF, and a comprehensive study of microseismicity by Y. Zhou et al. (2022) inferred that the XJF is in the late post-earthquake loading stage. The seismicity in the southern section of the RRF is relatively low, with no earthquakes *M*6.0 or above have occurred historically, and the small seismic activity is weak. It is worth noting that strong earthquakes have a tendency to move up the QJF and SJF. Since 1900, six earthquakes above *M*6.0 have cumulatively occurred on the QJF and SJF, with intensive small seismic activity. Consequently, the front edge of the SYB exhibits high seismicity.

The study area has experienced a lengthy geological process, resulting in the exposure of Paleoproterozoic to Cenozoic strata (Figure 1b). Within the SYB, the strata mainly consist of Mesoproterozoic phyllite, slate, quartzite, sandstone, and greywacke. These formations are overlain by Ordovician sandstone, conglomerate, Jurassic purplish-red sandstone, shale, mudstone, and Paleocene sandstone. The stratigraphy is complex and varied along the XJF, which exposes carbonate rock, sandstone, shale, mudstone, and phyllite. In addition, the Permian Emeishan Basalt and Cretaceous Gejiu Granite are locally exposed. The RRF has been subjected to strong tectonic deformation, owing to which gneiss, hornblende, syenite, marble, schist, hornblende, and other high-level Ailaoshan metamorphic rocks of the Paleoproterozoic have become exposed (C. Wang et al., 2021). Additionally, the RRF has experienced multiple granite vein intrusions during the Neoproterozoic, Triassic-Jurassic, and Cenozoic (W. Chen et al., 2018).

3. Data and Methods

In this study, field investigations were conducted in July and November 2022, and a total of 22 thermal spring water samples and seven bubbling gas samples were collected along the southern segment of the XJF, RRF, QJF, and SJF (Figure 1b). The temperature, pH value, and electrical conductivity (EC) of hot springs were measured using a portable multi-parameter water quality analyzer (ProfiLine pH/Cond 3320 WTW, Germany) with measurement accuracies of 0.1°C, 0.01, and 1 μS/cm, respectively. The WTW device was calibrated using standard solutions before measurement. Prior to sampling, high-density polyethylene (HDPE) bottles were washed three times with deionized water and rinsed twice with thermal water. Each thermal water sample was filtered using a 0.45 μm microporous membrane and collected in 100 mL HDPE bottles for major ions and SiO_2 concentration analysis; 30 mL HDPE bottles were used for hydrogen and oxygen isotope analysis. The thermal water samples for cation analysis required the addition of high-purity nitric acid solution for acidification. Care was taken to prevent the entry of air bubbles during water sample collection, and the samples were sealed and stored under refrigerated conditions (4°C). To collect bubbling gas, a gas-collection device based on the gas drainage collection method was used; the details of the sampling procedures have previously been described by C. Zhao et al. (2017). Gas samples for chemical composition analysis were collected in 500 mL aluminum foil gas sample bags, while gas samples for helium and carbon isotope composition analysis were collected in 125 mL sodium glass bottles. The glass bottles were filled with 25 mL of hot spring water and sealed with crimped rubber stoppers prior to storage upside down.

The concentrations of major cations (Na^+, K^+, Ca^{2+}, and Mg^{2+}) and anions (F^-, Cl^-, and SO_4^{2-}) of the hot spring samples were determined using an ion chromatograph (Metrohm 883 Basic IC plus) with a detection limit of 0.01 mg/L. The HCO_3^- and CO_3^{2-} concentrations were analyzed using volumetric titration (HCl titration method). The SiO_2 concentration was determined by silicon molybdenum yellow spectrophotometry using a visible spectrophotometer (T6, Xinyue). To ensure data accuracy, ion balance errors were checked for each sample, and all samples exhibited ion balances within ±5%. The gas compositions were analyzed using a gas chromatograph (GC) (Agilent 7890A) equipped with a liquid nitrogen cooling system. The precision of the gas composition analysis (V/V) was as follows: He (5 ppm) and CO_2 (0.5%). All of the aforementioned analysis procedures were conducted at the Deep Fluid Laboratory of Yunnan Earthquake Agency, the details of which can be found in a study by C. Zhao et al. (2017) and Q. Li et al. (2019).

The hydrogen (^2H) and oxygen (^{18}O) isotope compositions in the hot spring samples were determined using a high-precision water isotope analyzer (Picarro L2140-i, USA) at the Institute of Earthquake Forecasting, China Earthquake Administration. The results were reported in international standard δ notation per mil (‰) relative to Vienna Standard Mean Ocean Water. The measurement accuracies were $\delta^{18}O \le 0.03‰$ and $\delta^2H \le 0.10‰$, respectively. The He-C isotope composition of bubbling gas samples was analyzed at the Key Laboratory of Petroleum Resources Research, Institute of Geology and Geophysics, Chinese Academy of Sciences in Lanzhou, China. The $^3He/^4He$ and $^4He/^{20}Ne$ ratios were determined using a noble gas mass spectrometer (Nu Instruments, UK) in the static mode, with a relative standard deviation of <5%. The atmospheric sample from Gaolan Hill in the south of Lanzhou was used as the standard sample. The carbon isotopic values of CO_2 and CH_4 were analyzed using a GC-IRMS analytical system, which consists of an Agilent 6890 GC and a Thermo Fisher Delta Plus-XP stable isotope ratio mass spectrometer. The measurement error for the carbon isotopic ratios was ±0.3‰. The carbon isotopic ratios are expressed by the conventional δ notation per mil (‰) relative to Vienna Pee Dee Belemnite.

4. Results

4.1. Characteristics of Thermal Water

The ionic and isotopic compositions of thermal water in the study area are listed in Table S1 of Supporting Information S1. The water temperatures range from 25.0 to 97.0°C, with higher temperatures observed along the RRF. The pH values range from 6.33 to 9.98, indicating weak acidity to alkalinity of water. The EC values range from 367 to 2,550 μS/cm, and the total dissolved solids (TDS) range from 182 to 2,961 mg/L, indicating freshwater to slightly saline water. The concentrations of major cations, including Na^+, K^+, Ca^{2+}, and Mg^{2+}, range from 2.37 to 329.75 mg/L, 1.02–24.12 mg/L, 1.28–650.78 mg/L, and 0.04–73.90 mg/L, respectively. The concentrations of major anions, including HCO_3^-, CO_3^{2-}, Cl^-, and SO_4^{2-}, range from 56.37 to 928.73 mg/L, 9.90–56.35 mg/L, 0.15–67.30 mg/L, and 2.24–1742.19 mg/L, respectively. The SiO_2 concentration ranges from 14.46 to 144.46 mg/L. It should be noted that the thermal waters along the XJF have lower temperature values, EC, TDS, and SiO_2 compared to those along the RRF and the ICB.

The classification results of the major-ion composition of thermal water (Figure 2) show that the hydrochemical types of most thermal waters are HCO_3-Ca·Mg type along the XJF, except in the southern end of XJF, being the HCO_3-Na type. The cations exhibit no distinct cation-dominant end elements along the RRF, and the hydrochemical types are classified as SO_4-Ca·Na, SO_4·HCO_3-Ca·Na, and HCO_3-Ca·Na type; within the ICB, it is the HCO_3-Na type. The hydrochemical types are primarily controlled by the interaction between water and the surrounding aquifer rocks. In carbonate rock areas, the dissolution of limestone and dolomite forms HCO_3-Ca·Mg type water, while the dissolution of evaporites can lead to the formation of SO_4-Ca·Mg and SO_4·Cl-Na type water. In the metamorphic rock regions along the RRF, Na^+ and HCO_3^- could originate from the dissolution of sodium feldspar and plagioclase, while Ca^{2+} can be derived from the dissolution of anorthite, mica, and marble. The high concentration of SO_4^{2-} is likely from gypsum dissolution. Furthermore, hydrothermal pyrite formed under the control of ductile shear along the RRF (J. Deng et al., 2015), and SO_4^{2-} could also result from the oxidation of pyrite. HCO_3-Na type water is primarily distributed in sandstone and granite type areas (Figure 1). The primary water-rock interaction reactions can be summarized as follows:

$$CaCO_3(\text{calcite}) + H_2O + CO_2 \rightarrow 2HCO_3^- + Ca^{2+} \quad (1)$$

$$CaSO_4 \cdot 2H_2O(\text{gypsum}) \rightarrow 2H_2O + SO_4^{2-} + Ca^{2+} \quad (2)$$

$$2FeS_2(\text{ pyrite}) + 2H_2O + 7O_2 \rightarrow 2FeSO_4 + 2SO_4^{2-} + 4H^+ \quad (3)$$

$$CaMg(CO_3)_2(\text{dolomite}) + 2H_2O + 2CO_2 \rightarrow 4HCO_3^- + Ca^{2+} + Mg^{2+} \quad (4)$$

$$2NaAlSi_3O_8(\text{albite}) + 3H_2O + 2CO_2 \rightarrow H_4Al_2Si_2O_9 + 4SiO_2 + 2HCO_3^- + 2Na^+ \quad (5)$$

$$CaO \cdot 2Al_2O_3 \cdot 4SiO_2(\text{anorthite}) + 2CO_2 + 5H_2O \rightarrow 2H_4Al_2Si_2O_9 + 2HCO_3^- + Ca^{2+} \quad (6)$$

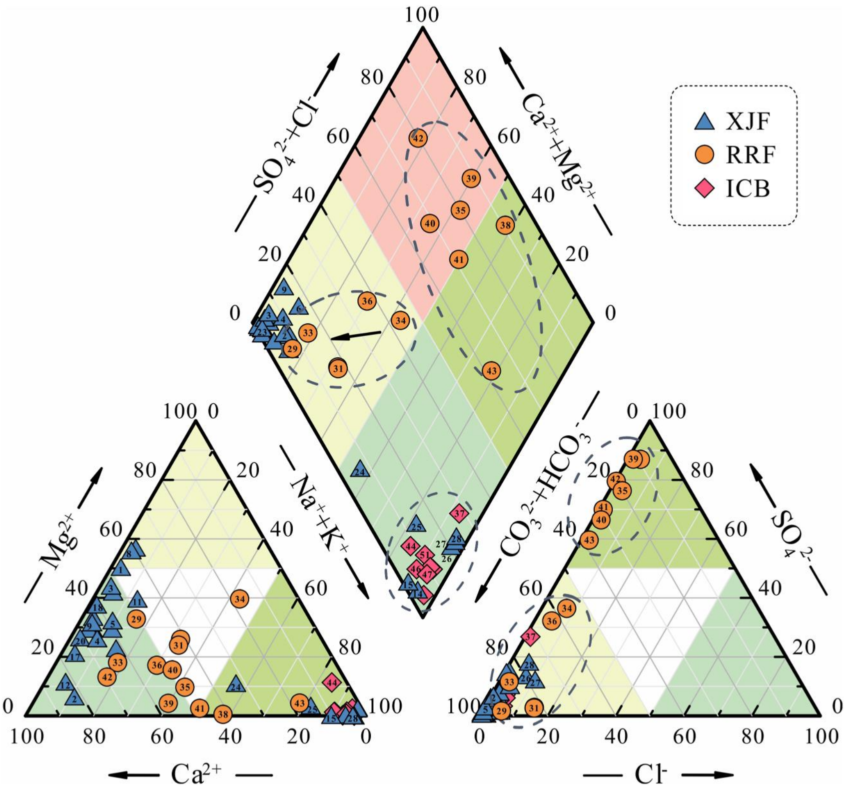

Figure 2. Piper diagram of thermal water from the study area (Piper, 1944).

Hydrogen and oxygen stable isotopes are widely used to study groundwater circulation and trace water sources, analyze water-rock reactions, evaluate the evaporation process, determine water mixing, and estimate recharge elevation (Pang et al., 2017; L. Zhang et al., 2021). The ranges of δ^2H and $\delta^{18}O$ values along the XJF are −96.81‰ to −78.55‰ and −12.96‰ to −10.50‰, respectively. For the RRF, the ranges of δ^2H and $\delta^{18}O$ values are −74.99‰ to −59.20‰ and −10.84‰ to −8.30‰, respectively. All of them fall along the Local Meteoric Water Line (G. Li et al., 2016) and the Global Meteoric Water Line (Craig, 1961), indicating an insignificant shift in δ^2H and $\delta^{18}O$ values (Figure 3). This suggests that the thermal spring waters are recharged by atmospheric precipitation and may not have experienced intense or prolonged water-rock interactions or slight effects of exchange with CO_2 (Joseph et al., 2011; Pang et al., 2017), resulting in insignificant $\delta^{18}O$ shift, which needs further exploration. Additionally, a noticeable isotopic elevation effect is observed, with the δ^2H and $\delta^{18}O$ values of thermal water becoming more negative as the sampling points increase in elevation.

4.2. Characteristics of Gases

The results of the 26 gas samples collected in the study area (Table S2 in Supporting Information S1) show that the He concentration varies greatly, ranging from 33 to 2,575 ppm, and the $^3He/^4He$ (R/Ra) ratios range from 0.02 to 0.67Ra. The $^4He/^{20}Ne$ ratios range from 1.42 to 168.29, which is much higher than the atmospheric ratio (0.318). The CO_2 concentration is relatively low, ranging from 0.09% to 42.52%, and the $\delta 13C_{CO2}$ values range from −24.39‰ to −6.53‰.

5. Discussion

5.1. Spatial Variations and Evolution of Thermal Water Geochemistry

In non-volcanic areas, groundwater generally undergoes a deep circulation through faults and is then heated by deep surrounding rocks to form hot springs. The results of hydrogen and oxygen isotopes indicate that the thermal water originates from atmospheric precipitation. The ion composition is primarily controlled by the lithology of

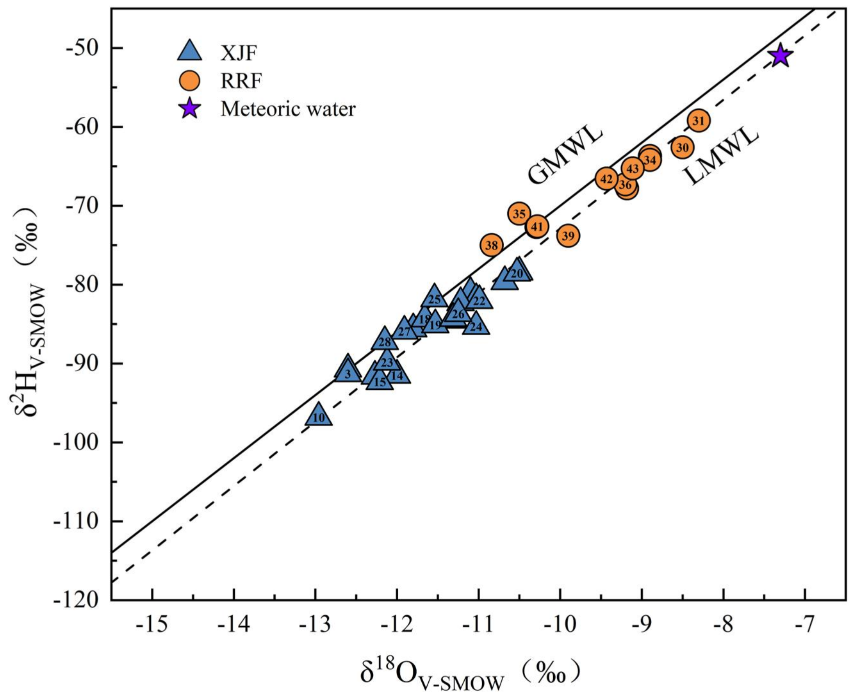

Figure 3. Plot of δ^2H versus $\delta^{18}O$ for thermal water and local meteoric water obtained from the study area. GMWL: the Global Meteoric Water Line, $\delta^2H = 8\delta^{18}O + 10$ (Craig, 1961); LMWL: the Local Meteoric Water Line (LMWL), $\delta^2H = 8.16\delta^{18}O + 8.7$, the LMWL and meteoric water in Mengzi City are according to G. Li et al. (2016) in this study.

the surrounding rocks, indicated by hydrochemical types. In this case, variations in the permeability of the fault zone could play a crucial role in modifying the hydrochemical characteristics.

Based on the hydrochemical types and surrounding rock lithology at the front edge of the SYB, Ca^{2+}, and HCO_3^- are the dominant ions in thermal water, and their concentrations are susceptible to water-rock interactions. High concentrations of Ca^{2+}, HCO_3^-, and TDS are observed along the RRF and the western side of the XJF, particularly in the QJF and SJF subordinate faults (Figures 7b–7d). The average concentrations of Ca^{2+}, HCO_3^-, and TDS in the RRF reach remarkably high levels of 180.43, 405.55, and 1066.13 mg/L, respectively. In comparison, the average concentrations of Ca^{2+}, HCO_3^-, and TDS in the QJF and SJF (108.36, 607.32, and 527.54 mg/L, respectively) are significantly higher (~2 times) than those in the XJF (50.90, 279.61, and 271.18 mg/L, respectively). RRF is a large-scale boundary fault, which provides pathways conducive to water circulation. Previous studies have shown that increases in the ion concentration are a result of regional stress accumulations, which promote the development of pore spaces within faults and enhance the intensity of water-rock reactions (Rosen et al., 2018; Woith et al., 2013). Research on surface permeability has revealed that tectonic settings exert stronger control on the permeability of near-surface (within ~0.4 km) crystalline rocks compared to deeper regions (Earnest & Boutt, 2014; Ranjram et al., 2015). Therefore, the higher ion concentrations observed along the QJF and SJF indicate that these faults are subjected to more intense regional compression than the southern segment of the XJF. Furthermore, despite the fact that RRF has high ion concentrations, the hydrochemical types of the RRF exhibit a distinct transition toward the HCO_3-Ca·Mg type (Figure 2) on the western side of the XJF, which could also be attributed to the compressive forces exerted on the front edge of the SYB, resulting in water mixing.

As major conduits, active faults play a crucial role in the fluid migration, and previous studies have reported numerous cases of water mixing in fault intersection zones (Gómez Díaz & Mariño Arias, 2020; Sabri et al., 2019; Shoedarto et al., 2021). A clear distinction exists between the HCO_3-Na type water at the southern end of the XJF and the $SO_4 \cdot HCO_3$-Ca·Na type water along the RRF in the Piper diagram rhombic area (Figure 2), and no mixing trend is observed. Moreover, conservative elements (Cl^-, B^-, Sr^{2+}) are widely used in groundwater mixing studies because of the accumulation of concentration during water-rock reactions and leaching and are not easily attenuated by precipitation or exchange (Stefánsson et al., 2019; T. Zheng et al., 2023). The relatively low Cl^-

10.1029/2023GC011431

concentration indicates that the thermal water in our study area emerges at the surface after atmospheric precipitation circulating through fractures, without being mixed with high Cl^- water sources, such as deep brine or ancient seawater. The δ^2H-$\delta^{18}O$ values are less influenced by factors such as H_2S exchange, seawater mixing, or evaporation in non-volcanic regions with inland humidity. Furthermore, δ^2H values are insignificantly affected during water-rock reactions, except at very high rock-water ratios. Consequently, the Cl^- and δ^2H relationship can effectively indicate the water mixing process. As the Cl^- increases, a gradual difference in δ^2H values is observed, the thermal water along the XJF exhibits a trend of enhanced water-rock interactions, and the thermal water on the RRF could be a combination of both water-rock interactions and surface leaching water (Figure 4). Based on the aforementioned results, the groundwater at the intersection of the XJF and the RRF exhibits distinct evolutionary trends, and there is no evidence of mixing, which proves that there is no interconnected pathway between the XJF and the RRF.

Most thermal water in the Na-K-Mg ternary diagram (Figure 5) is plotted in the immature water zone with high Mg^{2+} concentrations, which indicates that the thermal water is mixed with varying proportions of shallow cold water. The cold water mixing percentages for thermal water from the XJF range from 60% to 93% and 64%–92% for thermal water from the RRF (Table S1 in Supporting Information S1) estimated by the dissolved silica versus enthalpy model (Figure S1 in Supporting Information S1) (Fournier & Truesdell, 1974; Truesdell & Fournier, 1977). Similarly, thermal water at the same isotherm could indicate the mixing of deep source geothermal fluids and shallow groundwater at the same fault, and these deep source reservoir temperatures are ~160°C in the XJF and ~240°C in the RRF. Considering dilution by shallow cold water mixing, the cation system of the thermal water is in a non-equilibrium state; therefore, the results obtained from cation ratio thermometers may not be accurate enough. The quartz geothermometer (Fournier, 1977) provides the lowest estimate of reservoir temperature and the dissolved silica versus enthalpy model provides the reservoir temperature before cold water mixing (Table S1 in Supporting Information S1), and the reservoir temperature field was derived from a Kriging interpolation fit (Figure 7d). Although the contribution of radiogenic heat from granitic sources cannot be completely disregarded, the reservoir temperatures in ICB exhibit generally high and relatively small variations, indicating a stable reservoir temperature field in ICB. On the other hand, the distributions of reservoir temperatures in the front of the SYB are highly uneven, with large variations and distinct transitional gradients.

5.2. Origins and Spatial Distributions of Gas Geochemistry

Helium, a noble gas, can serve as an indicator of the origins of deep fluids, specifically in distinguishing between crustal and mantle-derived fluids. This is possible due to the substantial differences in $^3He/^4He$ ratios observed in various reservoirs, such as the mantle (~8 Ra), crust (~0.02 Ra), and atmosphere (1 Ra) (Sano & Wakita, 1985). In addition to degassing from the primordial mantle, the higher $^3He/^4He$ ratios can be influenced by various factors. For instance, ^3He can originate from nuclear bomb decay, the decay of Li in the crust, and atmospheric contamination (Yokoyama et al., 1999). However, apart from atmospheric contamination during sampling and testing, the contribution from these sources of decay is overshadowed by the dominant role of mantle-derived He (Bai et al., 2023; S. Xu et al., 2022). The ternary mixing plot of mantle, crust, and air (Figure 6a) shows that gases with lower $^4He/^{20}Ne$ ratios are contaminated by approximately 20% air, which interferes with the actual $^3He/^4He$ ratios. Additionally, the $^3He/^4He$ ratios can also be influenced by the presence of ^4He produced from the decay of U and Th in the crust. Therefore, air correction is applied to the gases using the $^4He/^{20}Ne$ ratios, and gases with $^3He/^4He$ (Rc/Ra) > 0.2 Ra, representing ~2% mantle He contribution, are considered to have a reliable mantle He contribution.

The $^3He/^4He$ (Rc/Ra) ratios in the study area range from 0.03 to 0.59 Ra (Table S2 in Supporting Information S1). A clear classification phenomenon can be observed: thermal springs with $^3He/^4He$ (Rc/Ra) ratios exceeding 0.2 Ra are mainly distributed along the RRF, QJF, and SJF (Figures 6a and 7a), providing evidence for the mantle-derived helium contribution to these fault systems. In contrast, the gases along the southern segment of the XJF and in the IBC exhibit $^3He/^4He$ ratios below 0.2 Ra, indicating a predominant crustal degassing origin. Active faults serve as the main pathways for deep degassing in the Earth (Caracausi & Sulli, 2019; Chang et al., 2021; Y. Li et al., 2023), and the enrichment of $^3He/^4He$ is direct evidence of deep connectivity and material exchange along faults. Consequently, the observed spatial distribution variations in $^3He/^4He$ ratios suggest that the RRF, QJF, and SJF either extend into the mantle or experience the upwelling of mantle-derived materials within the crust. Based on previous geophysical and geochemical observations(Sun et al., 2014; M. Xu et al., 2006; X. Zhou et al., 2020), the higher $^3He/^4He$ ratios along the RRF suggest that it is a deep fault that cuts through the crust. The

10.1029/2023GC011431

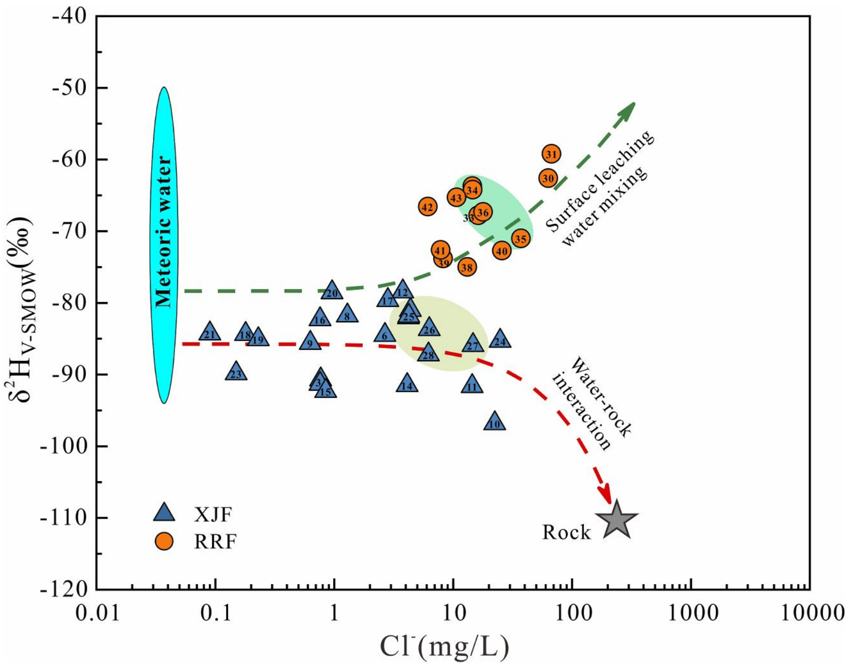

Figure 4. Relationships between δ^2H and Cl^- of thermal water from the study area (modified from T. Zheng et al. (2023)). The yellow zone and blue zone reflect thermal water from the intersection area of Xiaojiang fault and Red River fault.

magnetotelluric results (Figure 7a) indicate the possible presence of deep material upwelling within the crust on the western side of the XJF, which (Ye et al., 2022) speculated to be partially melted hydrous fluids from the mantle source. These confirm the results of higher mantle He contributions detected along the QJF and SJF. In contrast, the lower $^3He/^4He$ ratios may be attributed to the lack of active faults conducive to deep degassing. The

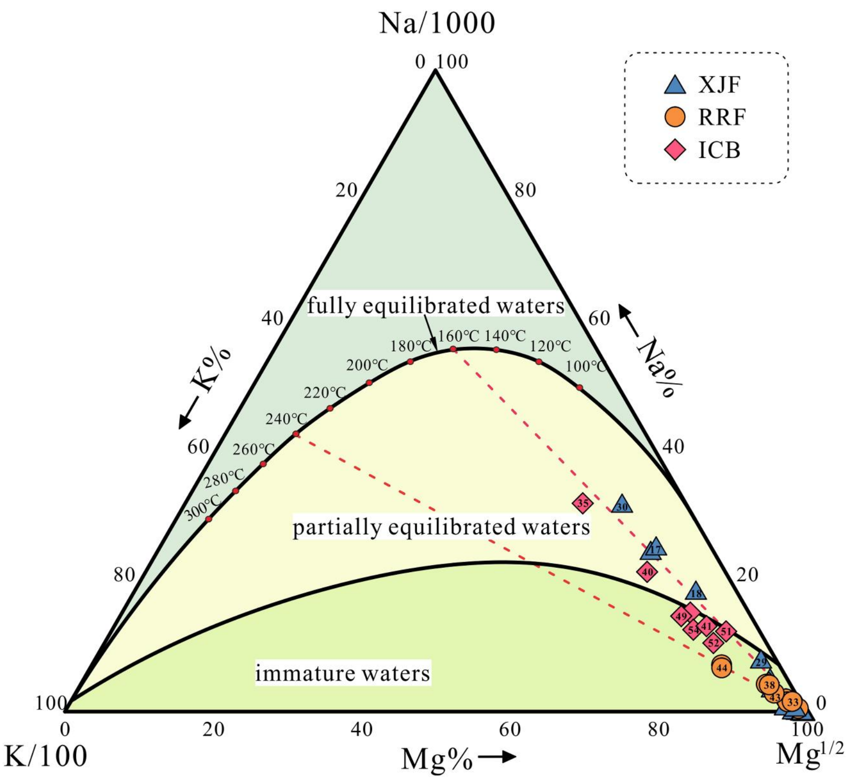

Figure 5. Na-K-Mg triangular diagram of thermal water samples in the study area (Giggenbach, 1988).

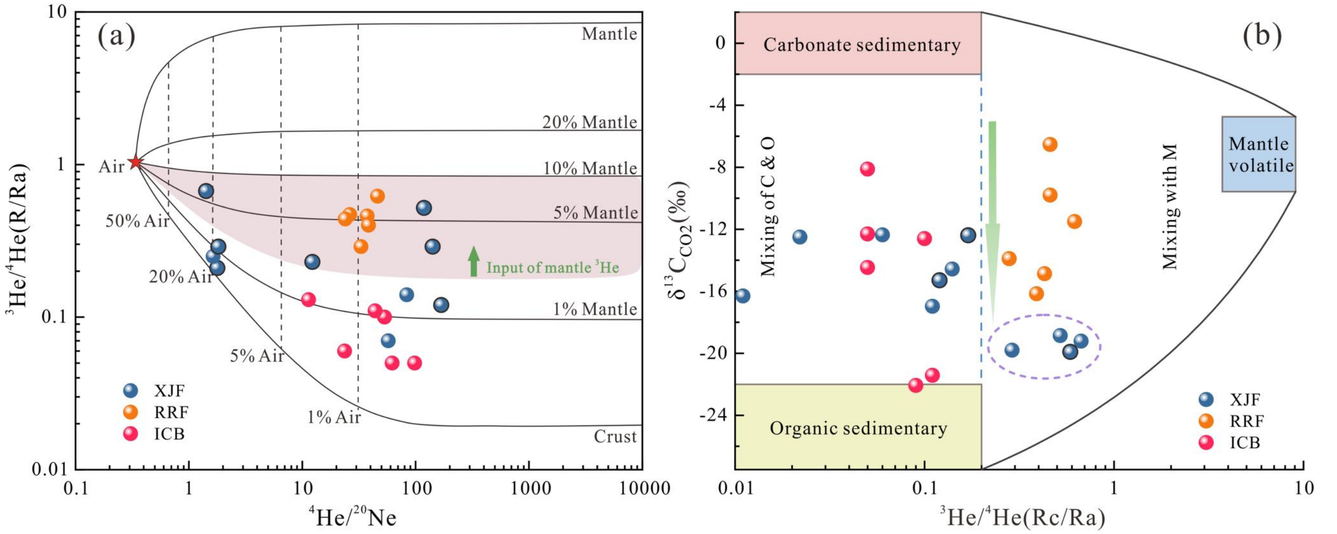

Figure 6. Correlation among isotope values of bubbling gas samples in the study area. (a) $^3He/^4He$ (R/Ra) versus $^4He/^{20}Ne$, $(R/Ra)_{Air}$ = 1.0 Ra, $(^4He/^{20}Ne)_{Air}$ = 0.318, $(R/Ra)_{Mantle}$ = 8.0 Ra, $(^4He/^{20}Ne)_{Mantle}$ = 1,000, $(R/Ra)_{Crust}$ = 0.02 Ra, $(^4He/^{20}Ne)_{Crust}$ = 1,000 (Sano & Wakita, 1985); (b) $\delta^{13}C_{CO2}$ versus $^3He/^4He$ (Rc/Ra) (modified from Tian et al. (2021)). The circle with a black line represents the data from this study. The circle without a black line represents data from previous studies.

convergence zone of large boundary faults promotes fracture development and enhances deep degassing processes (W. Liu et al., 2023; Yuce et al., 2017). However, the southern end of the XJF has lower $^3He/^4He$ ratios, with a value of only 0.06 for gas at No. 28. Previous studies have found a high-velocity body in the middle-lower crust at the intersection of the XJF and the RRF (S. Liu et al., 2022; Y. Xu et al., 2013; Yang et al., 2020), which hinders the southward movement of the XJF. Therefore, the southern end of the XJF may not have extended deep into the mantle or connected with the RRF that cuts through the crust.

CO_2 is considered to be the main carrier for He migration in the crust (Lee et al., 2019; W. Liu et al., 2023). The sources of CO_2 include mantle degassing, carbonate dissolution, metamorphic decarbonization, organic matter decomposition, and soil respiration (Ramnarine et al., 2012; S. Xu et al., 2022); each of these sources has specific ranges of isotopic compositions. The ratios of $^3He/^4He$ (Rc/Ra) versus $\delta^{13}C_{CO2}$ (Figure 6b) show that crustal-sourced gases have $\delta^{13}C_{CO2}$ values ranging from −22.07 to −8.12‰, indicating a potential mixture of multiple sources. Gases with mantle-derived He contributions are constrained to a narrow range of $^3He/^4He$ ratios, while the $\delta^{13}C_{CO2}$ values vary widely, from −19.93‰ to −6.53‰. The gases' $\delta^{13}C_{CO2}$ values from the RRF range from −16.16 to −6.53‰, which are primarily of mantle origin (−6.5‰±2.5‰ according to Sano and Marty (1995)), with some negative $\delta^{13}C_{CO2}$ values being related to gas mixing or CO_2 consumption through calcite precipitation (W. Liu et al., 2023; S. Xu et al., 2022). The gases' $\delta^{13}C_{CO2}$ values from the QJF and SJF range from −19.93‰ to −16.30‰, indicating the potential presence of shallow biogenic CO_2 (−25‰±3‰) (Robinson & Scrimgeour, 1995) mixed in. For gases with mantle-derived He contributions exceeding 2%, there is a transition from mantle-derived CO_2 to shallow biogenic CO_2 from the RRF to the QJF and SJF (Figure 6b). This indicates that the contribution of shallow gas components to the gases at the front edge of the SYB is greater than those in the RRF and ICB.

5.3. Tectonic Features Revealed by Fluid Geochemistry

The tectonic evolution of the SYB on the southeastern margin of the Tibetan Plateau is influenced by the Indian-Asia continental collision and subduction, block extrusion, and material rotational escape. The limited movement of the front edge of the SYB has resulted in spatial variations in the fluid distribution. The interconnection between the deep gas emission and the geochemical characteristics of shallow thermal water provides insight into the current tectonic pattern of the front edge of the SYB.

The high shear strain observed along the XJF does not extend to the RRF, but rather weakens and deflects southwestward from the southern segment of the XJF (Figure 7b). It then transitions into crustal contraction and extension, forming a complex dilatational strain rate (Y. Li et al., 2019). The XJF experiences a sudden decrease

10.1029/2023GC011431

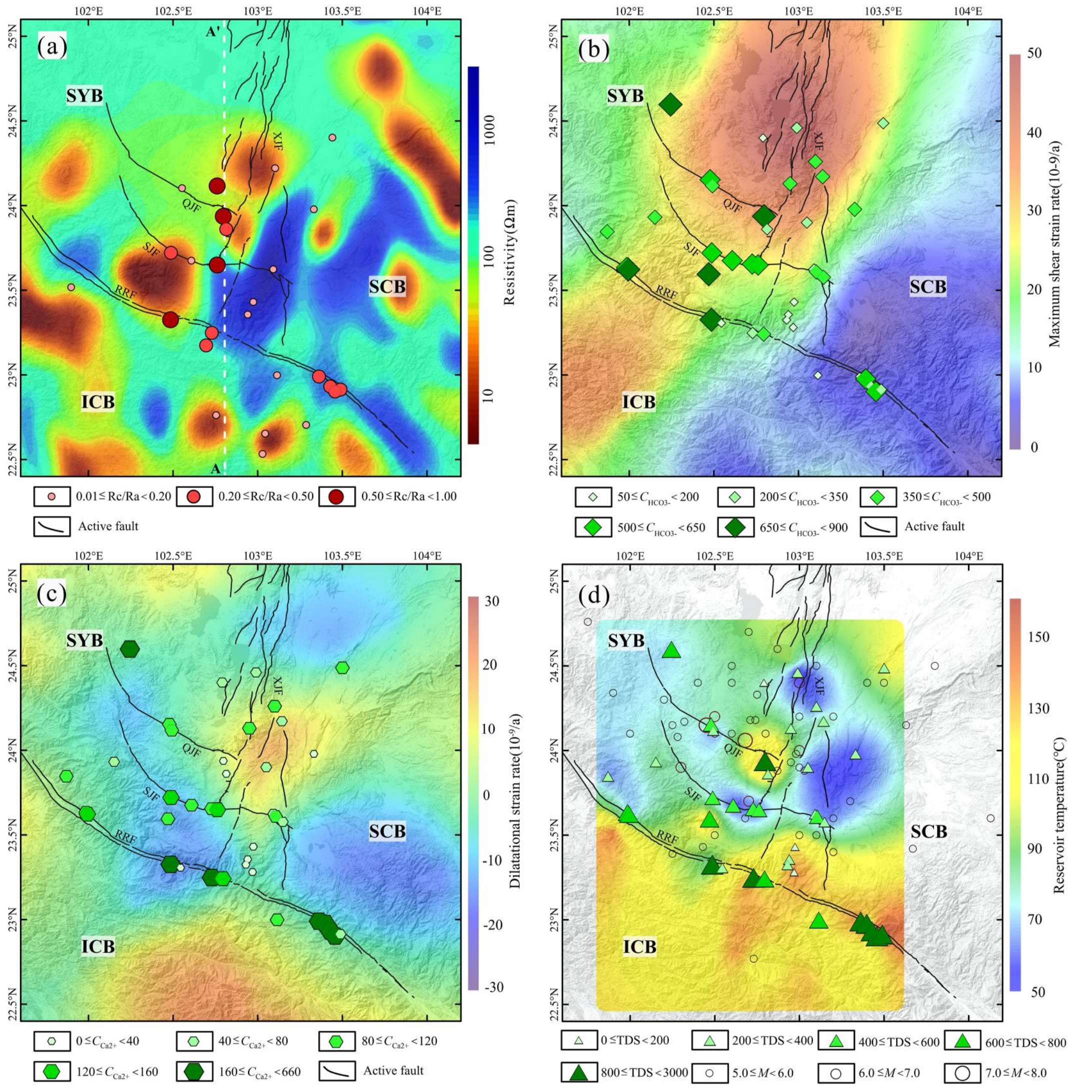

Figure 7. Spatial distribution of ion concentrations, total dissolved solids (TDS) values, $^3He/^4He$ (Rc/Ra) ratios, and earthquakes in the study area. (a) $^3He/^4He$ (Rc/Ra) ratios and resistivity; (b) HCO_3^- concentrations and maximum shear strain rate; (c) Ca^{2+} concentrations and dilatational strain rate; (d) TDS values, earthquakes, and reservoir temperature. Shear strain rate and dilatational strain rate data are according to Z. Li et al. (2020), and resistivity data are according to Yu et al. (2020). Earthquakes ($M \geq 5.0$) occurring since 1900 are from the National Earthquakes Data Center (https://data.earthquake.cn/).

when passing through the QJF, leading to right-lateral strike-slip and thrust along the QJF and the SJF (Z. Li et al., 2020; Wen et al., 2011). In terms of geological and geomorphological features, no significant displacements were found along the RRF that were cut through and dislocated by the XJF. Instead, the QJF, SJF, and RRF exhibit a geometric pattern of southwestward bending (Schoenbohm et al., 2006; Wen et al., 2022). The spatial variations in $^3He/^4He$ ratios can be explained by differences in fault-dependent permeability, extension, and seismic magnitude (Caracausi et al., 2022; W. Liu et al., 2023). Herein, the high hydrochemical ion concentrations and the presence of deep-derived gases along the RRF suggest that it still retains the features and functions as a block-boundary fault in the front edge of the SYB. The transition of hydrochemical types in the western section of the RRF can be interpreted as a result of the restricted movement of the SYB. The QJF and SJF exhibit distinctly higher concentrations of Ca^{2+}, HCO_3^-, and TDS, as well as mantle-derived He contributions, compared to the XJF. This suggests that these subordinate faults preferentially absorb the southward movement and energy from the XJF. Intense seismic activity, stress accumulation, compression, and fracturing lead to the opening of deep channels and an accelerated rate of water-rock reactions. Furthermore, the boundary effect of the southern

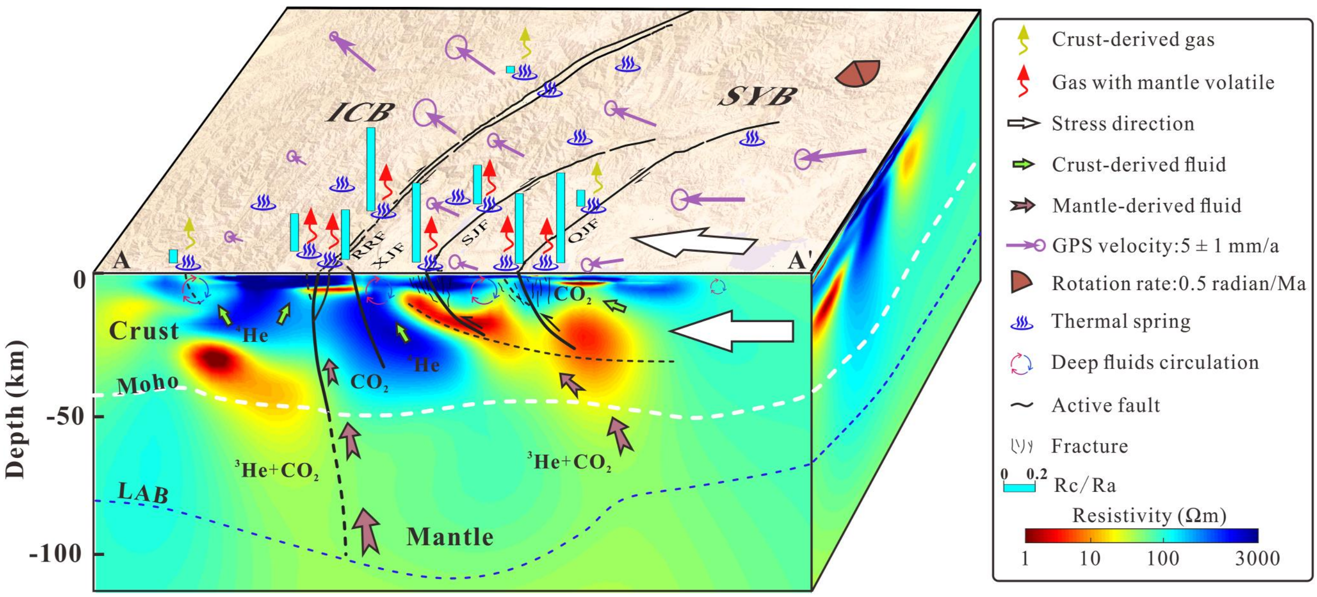

Figure 8. A schematic model showing 3D sketches of the tectonic features of the front edge of the Sichuan-Yunnan rhombic block (SYB). The resistivity data are according to Yu et al. (2020); Crustal thicknesses are according to T. Wu et al. (2016); the LAB is based on Hu et al. (2015); and the fault zones are according to Y. Wang, Zhang, et al. (2014) and Wen et al. (2022). GPS velocity field from Z. Li et al. (2020), with 1σ confidence level; and rotation rate of the SYB from Z .Shen et al. (2005).

section of the XJF is seen to be weakening. Spatial discrepancies in the reservoir temperature are related to stress levels, crustal thickness, fracture and cutting depth of faults, the activity level of faults, and the temperature of deep heat sources (Su et al., 2022). The spatial correlation between the dilatational strain rate and the reservoir temperature field (Figures 7c and 7d) further supports the strong relationship between the hydrochemistry of thermal water and regional strain.

In addition, compressive shear stresses are more favorable for faults to extend into depth and increase fault permeability, thus accelerating the release of mantle He (Faulkner et al., 2010; M. Zhang et al., 2021). Strong gas emissions have been observed along strike-slip and thrust faults in certain tectonic compression environments (Doğan et al., 2009; Klemperer et al., 2013). Beneath the QJF and SJF, thrust strike-slip faults exhibit lower P-wave and S-wave velocities (Bao et al., 2015; Yang et al., 2020), high-conductivity and low-resistivity bodies in the lower crust (Figure 7a), with high surface heat flow values (Jiang et al., 2019). The shear strain rates, seismicity, and deep fracture deformation in this area are more intense than those in other areas, and the development of new fractures within the faults may facilitate the transportation of mantle-derived gas from the trap. Therefore, the release of mantle-derived He along the QJF and SJF is the result of a combination of localized stress accumulation at the front edge of the SYB and upwelling of fluids from the depths (Figure 8). Under intense compression, new fractures or the reopening of pre-existing fractures can occur, leading to the further fracturing of shallow sedimentary layers (Z. Chen et al., 2022; Y. Li et al., 2023). The development of shallow fractures provides additional pathways for gas circulation, accelerating the cycling of gases. Thus, the detection of shallow biogenic CO_2 mixing along the QJF and SJF further confirms the enhanced compression activity.

Based on these findings, it can be inferred that the RRF still exhibits strong boundary effects, while the boundary effects may weaken along the southern segment of the XJF, with compressional stress transferring to the QJF and SJF subordinate faults in the front edge of the SYB. Further, this study shows that the XJF and RRF remain unconnected and have not formed pathways conducive to fluid transport. Therefore, it is speculated that the XJF does not cut through the RRF to the south, and its southward movement is restricted, leading to intense tectonic activity along the QJF and SJF subordinate faults at the front edge of the SYB. Fewer thermal springs with bubbling gas, lower gas $^3He/^4He$ ratios, lower shear strain rates, stable reservoir temperature fields, and extremely low historical seismicity in the ICB (Figure 7) indicate that the ICB is a stable block unaffected by extrusion, which is another reason for the XJF failing to cut through the RRF and moving southward (Figure 8).

Although stress accumulation occurs, the slip rate of subordinate faults on the west side of the XJF is lower. Nevertheless, the existence of ductile crust beneath these faults, enhanced fluid activity, and high pore pressures are more sensitive to shear stresses and slip rates (Lu et al., 2022). Deep-seated fluids can reduce the effective shear stress on faults, lower the mechanical strength of rocks, and decrease the friction between faults (W. Liu et al., 2023; Sano et al., 2014). The inhomogeneity of the reservoir temperature field and the upwelling of deep fluids possibly play an important role in the high frequency of seismic activity (W. Liu et al., 2022; Shao et al., 2022; Y. Wang et al., 2018). Therefore, deep fluids also provide conditions for the generation and triggering of earthquakes. In comparison, the ICB seems to be unaffected by this extrusion, and the future seismic hazard is relatively weaker than the front edge of the SYB. Furthermore, the higher peak ground acceleration in the front edge of the SYB, reaching 0.3 g along the QJF and SJF (Gao, 2015), the higher standards of seismic defense for buildings and continuous fluid geochemistry monitoring should be required.

6. Conclusions

In this study, the fluid geochemistry, deep geophysical imaging, and crustal deformation features along the principal active faults in the front edge of the SYB are investigated. Based on the results of this analysis, the following conclusions can be drawn:

1. Thermal spring water and gas exhibit a coupled spatial distribution relationship. Relatively high ion concentrations and $^3He/^4He$ ratios (Rc/Ra ratios of 0.21–0.62 Ra) are observed along the RRF, QJF, and SJF. Multidisciplinary results suggest that the RRF cuts through the crust, while there is a mantle-derived intrusion into the crust beneath the QJF and SJF. These active faults serve as pathways for mantle-derived fluid flow.
2. The spatial variations in the fluid distribution, tectonic activity, and surface deformation characteristics collectively reveal that the strong compressive stress shifts toward the western side of the XJF in the front edge of the SYB, accumulated on the QJF and SJF. The enhanced water-rock interactions and deep-derived gas degassing can be interpreted as the intense compressional deformation along these strike-slip and thrust faults, leading to the development of fractures.
3. The boundary effect of the RRF is stronger than that of the southern segment of the XJF in terms of the intensity of fluid geochemistry. The unmixing characteristics of fluids at the intersection of these two faults suggest the absence of conduits conducive to fluid migration between the faults. Combining the lower gas Rc/Ra ratios, lower shear strain rates, stable reservoir temperature field, and extremely low historical seismicity in the ICB, it is speculated that the current movement of the XJF may not cut through the RRF and continue southward. The future seismic activity at the front edge of the SYB still deserves attention, and the continuous monitoring of fluid geochemistry should be improved.

Data Availability Statement

The data of thermal spring water and gas chemical constituents (Shao, 2024) can be found at Mendeley Data, V1 (https://doi.org/10.17632/kxt9df6ngg.1).

Acknowledgments
This work was supported by the Key Research and Development Plan of Yunnan Province (No. 202203AC100003), the Project of Youth Fund for Earthquake Science of Yunnan Earthquake Agency (No. 2022K10), National Natural Science Foundation of China (No. 42073063), the Special Fund of the Institute of Earthquake Forecasting, China Earthquake Administration (No. CEAIEF20230301). This work is a contribution to IGCP Project 724. This manuscript has benefited from instructive comments by two anonymous reviewers. We also thank Prof. Xiaocheng Zhou, Dr. Jiao Tian, Dr. Shujuan Su, and Dr. Yucong Yan for their help with the water stable isotope analyses.

References

Allen, C. R., Gillespie, A. R., Han, Y. A., Sieh, K. E., Zhang, B. C., & Zhu, C. N. (1984). Red River and associated faults, Yunnan Province, China: Quaternary geology, slip rates, and seismic hazard. *Geological Society of America Bulletin*, *95*(6), 686–700. https://doi.org/10.1130/0016-7606(1984)95<686:Rraafy>2.0.Co;2

Bai, Y., Shi, Z., Zhou, X., Wu, C., Wang, G., He, M., et al. (2023). Gas geochemical evidence for the India-Asia lithospheric transition boundary near the Karakorum fault in western Tibet. *Chemical Geology*, *639*, 121728. https://doi.org/10.1016/j.chemgeo.2023.121728

Bao, X., Sun, X., Xu, M., Eaton, D. W., Song, X., Wang, L., et al. (2015). Two crustal low-velocity channels beneath SE Tibet revealed by joint inversion of Rayleigh wave dispersion and receiver functions. *Earth and Planetary Science Letters*, *415*, 16–24. https://doi.org/10.1016/j.epsl.2015.01.020

Bischoff, S. H., & Flesch, L. M. (2018). Normal faulting and viscous buckling in the Tibetan Plateau induced by a weak lower crust. *Nature Communications*, *9*(1), 4952. https://doi.org/10.1038/s41467-018-07312-9

Caracausi, A., Buttitta, D., Picozzi, M., Paternoster, M., & Stabile, T. A. (2022). Earthquakes control the impulsive nature of crustal helium degassing to the atmosphere. *Communications Earth & Environment*, *3*(1), 224. https://doi.org/10.1038/s43247-022-00549-9

Caracausi, A., & Sulli, A. (2019). Outgassing of mantle volatiles in compressional tectonic regime away from volcanism: The role of continental delamination. *Geochemistry, Geophysics, Geosystems*, *20*(4), 2007–2020. https://doi.org/10.1029/2018gc008046

Chang, L., Ying, L., Zhi, C., Zhaofei, L., Yuanxin, Z., Le, H., & Manning, A. H. (2021). Fluid geochemistry within the North China Craton: Spatial variation and genesis. *Geofluids*, *2021*, 1–17. https://doi.org/10.1155/2021/1009766

Chen, W., Liu, J., Fan, W., Feng, J., Yan, J., & Dao, H. (2018). Multiple stages of granitic dykes along the Ailao Shan-Red River shear zone: Constraints on timing of switch of shear strain types (in Chinese with English abstract). *Acta Petrologica Sinica*, *34*(5), 1347–1358.

Chen, Z., Li, Y., Liu, Z., He, H., Martinelli, G., Lu, C., & Gao, Z. (2022). Geochemical and geophysical effects of tectonic activity in faulted areas of the North China Craton. *Chemical Geology*, *609*, 121048. https://doi.org/10.1016/j.chemgeo.2022.121048

Chen, Z., Li, Y., Martinelli, G., Liu, Z., Lu, C., & Zhao, Y. (2020). Spatial and temporal variations of CO_2 emissions from the active fault zones in the capital area of China. *Applied Geochemistry*, *112*, 104489. https://doi.org/10.1016/j.apgeochem.2019.104489

Craig, H. (1961). Isotopic variations in meteoric waters. *Science*, *133*(346), 1702–1703. https://doi.org/10.1126/science.133.3465.1702

Deng, J., Wang, Q., Li, G., & Zhao, Y. (2015). Structural control and genesis of the Oligocene Zhenyuan orogenic gold deposit, SW China. *Ore Geology Reviews*, *65*, 42–54. https://doi.org/10.1016/j.oregeorev.2014.08.002

Deng, Q., Zhang, P., Ran, Y., Yang, X., Min, W., & Chu, Q. (2003). Basic characteristics of active tectonics of China (in Chinese with English abstract). *Science in China, Series D: Earth Sciences*, *46*(4), 356–372. https://doi.org/10.1360/03yd9032

Doğan, T., Sumino, H., Nagao, K., Notsu, K., Tuncer, M. K., & Çelik, C. (2009). Adjacent releases of mantle helium and soil CO_2 from active faults: Observations from the Marmara region of the North Anatolian Fault zone, Turkey. *Geochemistry, Geophysics, Geosystems*, *10*(11), Q11009. https://doi.org/10.1029/2009gc002745

Dong, S., Han, Z., Guo, P., Xie, Z., & Yin, X. (2023). Seismological research in Yunnan Province, China, and its tectonic implication between the Xianshuihe-Xiaojiang fault system and the Red River fault zone. *Frontiers in Earth Science*, *11*, 1239689. https://doi.org/10.3389/feart.2023.1239689

Earnest, E., & Boutt, D. (2014). Investigating the role of hydromechanical coupling on flow and transport in shallow fractured-rock aquifers. *Hydrogeology Journal*, *22*(7), 1573–1591. https://doi.org/10.1007/s10040-014-1148-7

Faulkner, D. R., Jackson, C. A. L., Lunn, R. J., Schlische, R. W., Shipton, Z. K., Wibberley, C. A. J., & Withjack, M. O. (2010). A review of recent developments concerning the structure, mechanics and fluid flow properties of fault zones. *Journal of Structural Geology*, *32*(11), 1557–1575. https://doi.org/10.1016/j.jsg.2010.06.009

Flesch, L. M., Haines, A. J., & Holt, W. E. (2001). Dynamics of the India-Eurasia collision zone. *Journal of Geophysical Research*, *106*(B8), 16435–16460. https://doi.org/10.1029/2001jb000208

Fournier, R. O. (1977). Chemical geothermometers and mixing models from geothermal systems. *Geothermics*, *5*(1), 41–50. https://doi.org/10.1016/0375-6505(77)90007-4

Fournier, R. O., & Truesdell, A. H. (1974). Geochemical indicators of subsurface temperature: Part 2, Estimation of temperature and fractions of hot water mixed with cold water. *Journal of Research of the U.S. Geological Survey*, *2*(3), 263–270.

Gao, M. (2015). *Promotion of teaching materials of seismic ground motion parameters zonation map of China (GB 18306-2015)* (in Chinese). Standards Press of China.

Giggenbach, W. F. (1988). Geothermal solute equilibria: Derivation of Na-K-Mg-Ca geoindicators. *Geochimica et Cosmochimica Acta*, *52*(12), 2749–2765. https://doi.org/10.1016/0016-7037(88)90143-3

Gómez Díaz, E., & Mariño Arias, O. M. (2020). Structural assessment and geochemistry of thermal waters at the Cerro Machin Volcano (Colombia): An approach to understanding the geothermal system. *Journal of Volcanology and Geothermal Research*, *400*, 106910. https://doi.org/10.1016/j.jvolgeores.2020.106910

Gori, F., & Barberio, M. D. (2022). Hydrogeochemical changes before and during the 2019 Benevento seismic swarm in central-southern Italy. *Journal of Hydrology*, *604*, 127250. https://doi.org/10.1016/j.jhydrol.2021.127250

Han, Z., Dong, S., Mao, Z., Hu, N., Tan, X., Yuan, R., & Guo, P. (2017). The Holocene activity and strike-slip rate of the southern segment of Xiaojiang fault in the southeastern Yunnan region, China (in Chinese with English abstract). *Seismology and Geology*, *39*(1), 1–19. https://doi.org/10.3969/j.issn.0253-4967.2017.01.001

He, H., Chen, Z., Liu, Z., Gao, Z., Hu, L., Lu, C., et al. (2023). Geochemical features of fluid in Xiaojiang fault zone, Southeastern Tibetan Plateau: Implications for fault activity. *Applied Geochemistry*, *148*, 105507. https://doi.org/10.1016/j.apgeochem.2022.105507

He, H., Fang, Z., & Li, P. (1993). A preliminary approach to the fault activity of southern segment on Xiaojiang west branch fault (in Chinese with English abstract). *Journal of Seismological Research*, *16*(03), 291–298.

Hosono, T., Yamada, C., Manga, M., Wang, C. Y., & Tanimizu, M. (2020). Stable isotopes show that earthquakes enhance permeability and release water from mountains. *Nature Communications*, *11*(1), 2776. https://doi.org/10.1038/s41467-020-16604-y

Hu, J., Yang, H., Li, G., & Peng, H. (2015). Seismic upper mantle discontinuities beneath Southeast Tibet and geodynamic implications. *Gondwana Research*, *28*(3), 1032–1047. https://doi.org/10.1016/j.gr.2014.08.016

Italiano, F., Yuce, G., Uysal, I. T., Gasparon, M., & Morelli, G. (2014). Insights into mantle-type volatiles contribution from dissolved gases in artesian waters of the Great Artesian Basin, Australia. *Chemical Geology*, *378–379*, 75–88. https://doi.org/10.1016/j.chemgeo.2014.04.013

Jiang, G., Hu, S., Shi, Y., Zhang, C., Wang, Z., & Hu, D. (2019). Terrestrial heat flow of continental China: Updated dataset and tectonic implications. *Tectonophysics*, *753*, 36–48. https://doi.org/10.1016/j.tecto.2019.01.006

Joseph, E. P., Fournier, N., Lindsay, J. M., & Fischer, T. P. (2011). Gas and water geochemistry of geothermal systems in Dominica, Lesser Antilles island arc. *Journal of Volcanology and Geothermal Research*, *206*(1–2), 1–14. https://doi.org/10.1016/j.jvolgeores.2011.06.007

Klemperer, S. L., Kennedy, B. M., Sastry, S. R., Makovsky, Y., Harinarayana, T., & Leech, M. L. (2013). Mantle fluids in the Karakoram fault: Helium isotope evidence. *Earth and Planetary Science Letters*, *366*, 59–70. https://doi.org/10.1016/j.epsl.2013.01.013

Kulongoski, J. T., Hilton, D. R., Barry, P. H., Esser, B. K., Hillegonds, D., & Belitz, K. (2013). Volatile fluxes through the Big Bend section of the San Andreas Fault, California: Helium and carbon-dioxide systematics. *Chemical Geology*, *339*, 92–102. https://doi.org/10.1016/j.chemgeo.2012.09.007

Lee, H., Kim, H., Kagoshima, T., Park, J. O., Takahata, N., & Sano, Y. (2019). Mantle degassing along strike-slip faults in the Southeastern Korean Peninsula. *Scientific Reports*, *9*(1), 15334. https://doi.org/10.1038/s41598-019-51719-3

Leloup, P. H., Lacassin, R., Tapponnier, P., Schärer, U., Zhong, D., Liu, X., et al. (1995). The Ailao Shan-Red River shear zone (Yunnan, China), Tertiary transform boundary of Indochina. *Tectonophysics*, *251*(1–4), 3–84. https://doi.org/10.1016/0040-1951(95)00070-4

Li, C., Zhou, X., Yan, Y., Ouyang, S., & Liu, F. (2021). Hydrogeochemical characteristics of hot springs and their short-term seismic precursor anomalies along the Xiaojiang Fault Zone, Southeast Tibet Plateau. *Water*, *13*(19), 2638. https://doi.org/10.3390/w13192638

Li, G., Zhang, X., Xu, Y., Song, S., Wang, Y., Ji, X., et al. (2016). Characteristics of stable isotopes in precipitation and their moisture sources in Mengzi Region, Southern Yunnan (in Chinese with English abstract). *Environmental Science*, *37*(4), 1313–1320. https://doi.org/10.13227/j.hjkx.2016.04.016

Li, Q., Wang, Y., Zhou, Y., & Zhao, C. (2019). Geothermal anomalies in the Jianchuan-Deqin region: Constraints on the northwest boundary of Sichuan-Yunnan rhombic block and seismic activity (in Chinese with English abstract). *Bulletin of Mineralogy, Petrology and Geochemistry*, *38*(1), 90–102. https://doi.org/10.19658/j.issn.1007-2802.2019.38.012

Li, Y., Chen, Z., Sun, A., Liu, Z., Caracausi, A., Martinelli, G., & Lu, C. (2023). Geochemical features and seismic imaging of the tectonic zone between the Tibetan Plateau and Ordos Block, central northern China. *Chemical Geology*, *622*, 121386. https://doi.org/10.1016/j.chemgeo.2023.121386

Li, Y., Du, J., Wang, X., Zhou, X., Xie, C., & Cui, Y. (2013). Spatial variations of soil gas geochemistry in the Tangshan area of northern China. *Terrestrial, Atmospheric and Oceanic Sciences*, *24*(3), 323–332. https://doi.org/10.3319/tao.2012.11.26.01(tt)

Li, Y., Liu, M., Li, Y., & Chen, L. (2019). Active crustal deformation in southeastern Tibetan Plateau: The kinematics and dynamics. *Earth and Planetary Science Letters*, *523*, 115708. https://doi.org/10.1016/j.epsl.2019.07.010

Li, Z., Gan, W., Qin, S., Hao, M., Liang, S., & Yang, F. (2019). Present-day deformation characteristics of the southeast borderland of the Tibetan Plateau (in Chinese with English abstract). *Chinese Journal of Geophysics*, *62*(12), 4540–4553. https://doi.org/10.6038/cjg2019M0692

Li, Z., Wang, Y., Gan, W., Fang, L., Zhou, R., Seagren, E. G., et al. (2020). Diffuse deformation in the SE Tibetan Plateau: New insights from geodetic observations. *Journal of Geophysical Research: Solid Earth*, *125*(10). https://doi.org/10.1029/2020jb019383

Li, Z., Zhou, X., Xu, Q., Yan, Y., He, M., Li, J., et al. (2022). Hydrochemical characteristics of hot springs in the intersection of the Red River fault zone and the Xiaojiang fault zone, Southwest Tibet Plateau. *Water*, *14*(16), 2525. https://doi.org/10.3390/w14162525

Liu, S., Chang, K., Yang, D., Xu, X., Wang, W., Yang, S., & Li, M. (2022). Velocity and azimuthal anisotropy structures beneath the Dianzhong Block and its vicinity, SE Tibetan Plateau, revealed by eikonal equation-based traveltime tomography. *Tectonophysics*, *839*, 229525. https://doi.org/10.1016/j.tecto.2022.229525

Liu, W., Guan, L., Liu, Y., Xie, X., Zhang, M., Chen, B., et al. (2022). Fluid geochemistry and geothermal anomaly along the Yushu-Ganzi-Xianshuihe fault system, eastern Tibetan Plateau: Implications for regional seismic activity. *Journal of Hydrology*, *607*, 127554. https://doi.org/10.1016/j.jhydrol.2022.127554

Liu, W., Zhang, M., Chen, B., Liu, Y., Cao, C., Xu, W., et al. (2023). Hydrothermal He and CO_2 degassing from a Y-shaped active fault system in eastern Tibetan Plateau with implications for seismogenic processes. *Journal of Hydrology*, *620*, 129482. https://doi.org/10.1016/j.jhydrol.2023.129482

Lu, W., Zhou, Y., Zhao, Z., Yue, H., & Zhou, S. (2022). Aftershock sequence of the 2017 Mw 6.5 Jiuzhaigou, China earthquake monitored by an AsA network and its implication to fault structures and strength. *Geophysical Journal International*, *228*(3), 1763–1779. https://doi.org/10.1093/gji/ggab443

Ma, L., Qiao, X., Min, L., Fa, B., & Ding, X. (2002). *Geological atlas of China* (pp. 1–348). Geology Press.

McGibbon, C., Crossey, L. J., Karlstrom, K. E., & Grulke, T. (2018). Carbonic springs as distal manifestations of geothermal systems, highlighting the importance of fault pathways and hydrochemical mixing: Example from the Jemez Mountains, New Mexico. *Applied Geochemistry*, *98*, 45–57. https://doi.org/10.1016/j.apgeochem.2018.08.015

Michel, G. W., Becker, M., Angermann, D., Reigber, C., & Reinhart, E. (2000). Crustal motion in E-and SE-Asia from GPS measurements. *Earth, Planets and Space*, *52*(10), 713–720. https://doi.org/10.1186/bf03352270

Moore, P. J., Martin, J. B., & Screaton, E. J. (2009). Geochemical and statistical evidence of recharge, mixing, and controls on spring discharge in an eogenetic karst aquifer. *Journal of Hydrology*, *376*(3–4), 443–455. https://doi.org/10.1016/j.jhydrol.2009.07.052

Pan, Y., & Shen, W. B. (2017). Contemporary crustal movement of southeastern Tibet: Constraints from dense GPS measurements. *Scientific Reports*, *7*(1), 45348. https://doi.org/10.1038/srep45348

Pang, Z., Kong, Y., Li, J., & Tian, J. (2017). An isotopic geoindicator in the hydrological cycle. *Procedia Earth and Planetary Science*, *17*, 534–537. https://doi.org/10.1016/j.proeps.2016.12.135

Piper, A. M. (1944). A graphic procedure in the geochemical interpretation of water-analyses. *Transactions, American Geophysical Union*, *25*(6), 914–928. https://doi.org/10.1029/tr025i006p00914

Ramnarine, R., Wagner-Riddle, C., Dunfield, K. E., & Voroney, R. P. (2012). Contributions of carbonates to soil CO_2 emissions. *Canadian Journal of Soil Science*, *92*(4), 599–607. https://doi.org/10.4141/cjss2011-025

Ranjram, M., Gleeson, T., & Luijendijk, E. (2015). Is the permeability of crystalline rock in the shallow crust related to depth, lithology or tectonic setting? *Geofluids*, *15*(1–2), 106–119. https://doi.org/10.1111/gfl.12098

Replumaz, A., Lacassin, R., Tapponnier, P., & Leloup, P. H. (2001). Large river offsets and Plio-Quaternary dextral slip rate on the Red River fault (Yunnan, China). *Journal of Geophysical Research*, *106*(B1), 819–836. https://doi.org/10.1029/2000jb900135

Ring, U., Uysal, I. T., Yüce, G., Ünal-İmer, E., Italiano, F., İmer, A., & Zhao, J. (2016). Recent mantle degassing recorded by carbonic spring deposits along sinistral strike-slip faults, south-central Australia. *Earth and Planetary Science Letters*, *454*, 304–318. https://doi.org/10.1016/j.epsl.2016.09.017

Robinson, D., & Scrimgeour, C. M. (1995). The contribution of plant C to soil CO_2 measured using $\delta^{13}C$. *Soil Biology and Biochemistry*, *27*(12), 1653–1656. https://doi.org/10.1016/0038-0717(95)00109-r

Rosen, M. R., Binda, G., Archer, C., Pozzi, A., Michetti, A. M., & Noble, P. J. (2018). Mechanisms of earthquake-induced chemical and fluid transport to carbonate groundwater springs after earthquakes. *Water Resources Research*, *54*(8), 5225–5244. https://doi.org/10.1029/2017wr022097

Sabri, K., Marrero-Diaz, R., Ntarmouchant, A., Bento dos Santos, T., Ribeiro, M. L., Solá, A. R., et al. (2019). Geology and hydrogeochemistry of the thermo-mineral waters of the South Rif Thrust (Northern Morocco). *Geothermics*, *78*, 28–49. https://doi.org/10.1016/j.geothermics.2018.11.005

Sano, Y., Hara, T., Takahata, N., Kawagucci, S., Honda, M., Nishio, Y., et al. (2014). Helium anomalies suggest a fluid pathway from mantle to trench during the 2011 Tohoku-Oki earthquake. *Nature Communications*, *5*(1), 3084. https://doi.org/10.1038/ncomms4084

Sano, Y., & Marty, B. (1995). Origin of carbon in fumarolic gas from island arcs. *Chemical Geology*, *119*(1–4), 265–274. https://doi.org/10.1016/0009-2541(94)00097-r

Sano, Y., & Wakita, H. (1985). Geographical distribution of $^3He/^4He$ ratios in Japan: Implications for arc tectonics and incipient magmatism. *Journal of Geophysical Research*, *90*(B10), 8729–8741. https://doi.org/10.1029/jb090ib10p08729

Schoenbohm, L. M., Burchfiel, B. C., Liangzhong, C., & Jiyun, Y. (2006). Miocene to present activity along the Red River fault, China, in the context of continental extrusion, upper-crustal rotation, and lower-crustal flow. *Geological Society of America Bulletin*, *118*(5–6), 672–688. https://doi.org/10.1130/b25816.1

Shao, W. (2024). Hydrochemical properties and major chemical constituents of water samples and chemical and isotopic data of gas samples from the thermal springs in the intersection between the Xiaojiang fault and the Red River fault [Dataset]. Mendeley Data, V1. https://doi.org/10.17632/kxt9df6ngg.1

Shao, W., Wang, Y., Li, Q., & Fan, S. (2022). A study on hydrogeochemistry and tectonic activity features of hot springs in the Red River fault zone (in Chinese with English abstract). *Bulletin of Mineralogy, Petrology and Geochemistry*, *41*(3), 612–624. https://doi.org/10.19658/j.issn.1007-2802.2022.41.023

Shen, L., Yuan, D., Ding, T., Li, Y., Le, G., & Lin, Y. (2007). Distributing inhomogeneity of helium isotope of CO_2 degasification point and its geotectogenesis in southwest of China (in Chinese with English abstract). *Acta Geologica Sinica*, *81*(4), 475–487.

Shen, Z., Lü, J., Wang, M., & Bürgmann, R. (2005). Contemporary crustal deformation around the southeast borderland of the Tibetan Plateau. *Journal of Geophysical Research*, *110*(B11), B11409. https://doi.org/10.1029/2004jb003421

Shi, Z., & Wang, G. (2017). Evaluation of the permeability properties of the Xiaojiang Fault Zone using hot springs and water wells. *Geophysical Journal International*, *209*(3), 1526–1533. https://doi.org/10.1093/gji/ggx113

Shoedarto, R. M., Tada, Y., Kashiwaya, K., Koike, K., Iskandar, I., Malik, D., & Bratakusuma, B. (2021). Investigation of meteoric water and parent fluid mixing in a two-phase geothermal reservoir system using strontium isotope analysis: A case study from Southern Bandung, West Java, Indonesia. *Geothermics*, *94*, 102096. https://doi.org/10.1016/j.geothermics.2021.102096

Skelton, A., Andrén, M., Kristmannsdóttir, H., Stockmann, G., Mörth, C., Sveinbjörnsdóttir, Á., et al. (2014). Changes in groundwater chemistry before two consecutive earthquakes in Iceland. *Nature Geoscience*, *7*(10), 752–756. https://doi.org/10.1038/ngeo2250

Song, F., Wang, Y., Yu, W., Cao, Z., Shen, X., & Shen, J. (1998). *The active Xiaojiang fault zone*. Seismological Press. (in Chinese).

Stefánsson, A., Arnórsson, S., Sveinbjörnsdóttir, Á. E., Heinemaier, J., & Kristmannsdóttir, H. (2019). Isotope (δD, $\delta^{18}O$, ^{3}H, $\delta^{13}C$, ^{14}C) and chemical (B, Cl) Constrains on water origin, mixing, water-rock interaction and age of low-temperature geothermal water. *Applied Geochemistry*, *108*, 104380. https://doi.org/10.1016/j.apgeochem.2019.104380

Su, S., Li, Y., Chen, Z., Chen, Q., Liu, Z., Lu, C., & Hu, L. (2022). Geochemistry of geothermal fluids in the Zhangjiakou-Penglai Fault Zone, North China: Implications for structural segmentation. *Journal of Asian Earth Sciences*, *230*, 105218. https://doi.org/10.1016/j.jseaes.2022.105218

Sun, X., Bao, X., Xu, M., Eaton, D. W., Song, X., Wang, L., et al. (2014). Crustal structure beneath SE Tibet from joint analysis of receiver functions and Rayleigh wave dispersion. *Geophysical Research Letters*, *41*(5), 1479–1484. https://doi.org/10.1002/2014gl059269

Tapponnier, P., Peltzer, G., Le Dain, A. Y., Armijo, R., & Cobbold, P. (1982). Propagating extrusion tectonics in Asia: New insights from simple experiments with plasticine. *Geology*, *10*(12), 611. https://doi.org/10.1130/0091-7613(1982)10<611:Petian>2.0.Co;2

Tian, J., Pang, Z., Liao, D., & Zhou, X. (2021). Fluid geochemistry and its implications on the role of deep faults in the genesis of high temperature systems in the eastern edge of the Qinghai Tibet Plateau. *Applied Geochemistry*, *131*, 105036. https://doi.org/10.1016/j.apgeochem.2021.105036

Tong, Y., Yang, Z., Wang, H., Gao, L., An, C., Zhang, X., & Xu, Y. (2015). The Cenozoic rotational extrusion of the Chuan Dian Fragment: New paleomagnetic results from Paleogene red-beds on the southeastern edge of the Tibetan Plateau. *Tectonophysics*, *658*, 46–60. https://doi.org/10.1016/j.tecto.2015.07.007

Truesdell, A. H., & Fournier, R. O. (1977). Procedure for estimating the temperature of a hot-water component in a mixed water by using a plot of dissolved silica versus enthalpy. *Journal of Research of the U.S. Geological Survey*, *5*(1), 49–52.

Wang, C., Wang, Y., Zhang, Y., Qian, X., Zheng, Y., & Gou, Q. (2021). Magmatic-hydrothermal origin for Carlin-type Au deposits: Evidences from in-situ S-Pb isotopic compositions of sulfides, the Chang'an Au deposit, southern Ailaoshan tectonic zone. *Ore Geology Reviews*, *138*, 104372. https://doi.org/10.1016/j.oregeorev.2021.104372

Wang, E., Burchfiel, B. C., Royden, L. H., Chen, L., Chen, J., Li, W., & Chen, Z. (1998). *Late Cenozoic Xianshuihe-Xiaojiang, Red River, and Dali fault systems of southwestern Sichuan and central Yunnan, China*. Geological Society of America. https://doi.org/10.1130/0-8137-2327-2.1

Wang, Y. (2021). *A research on geochemical characteristics of geothermal fluids in Southeast Yunnan Province, China* (in Chinese with English abstract). Institute of Geophysics, China Earthquake Administration. https://doi.org/10.27487/d.cnki.gzdws.2021.000011

Wang, Y., Li, Q., Ran, H., Zhao, C., & Liu, Y. (2018). Geothermal and seismic activities in the southeastern Tibetan Plateau: Constraints from helium isotopes (in Chinese with English abstract). *Bulletin of Mineralogy, Petrology and Geochemistry*, *37*(4), 653–662. https://doi.org/10.19658/j.issn.1007-2802.2018.37.103

Wang, Y., Liu, Y., Zhao, C., Li, Q., Zhou, Y., & Ran, H. (2020). Helium and carbon isotopic signatures of thermal spring gases in southeast Yunnan, China. *Journal of Volcanology and Geothermal Research*, *402*, 106995. https://doi.org/10.1016/j.jvolgeores.2020.106995

Wang, Y., Zhang, B., Hou, J., & Xu, X. (2014). Structure and tectonic geomorphology of the Qujiang fault at the intersection of the Ailao Shan-Red River fault and the Xianshuihe-Xiaojiang fault system, China. *Tectonophysics*, *634*, 156–170. https://doi.org/10.1016/j.tecto.2014.07.031

Wang, Y., Zhao, C., Liu, F., Chen, K., & Ran, H. (2014). Research on relationship between geochemical characteristics of thermal springs and seismic activity in Xiaojiang fault zone and its adjacent area (in Chinese with English abstract). *Journal of Seismological Research*, *37*(2), 228–243.

Wen, X., Du, F., Long, F., Fan, J., & Zhu, H. (2011). Tectonic dynamics and correlation of major earthquake sequences of the Xiaojiang and Qujiang-Shiping fault systems, Yunnan, China. *Science China Earth Sciences*, *54*(10), 1563–1575. https://doi.org/10.1007/s11430-011-4231-0

Wen, X., Ma, S., Fang, L., Liang, M., Du, F., Long, F., & Zhao, X. (2022). Complex structural fault system and distributed deformation across the Big Bend of the Red River fault, Yunnan, China. *Physics of the Earth and Planetary Interiors*, *333*, 106942. https://doi.org/10.1016/j.pepi.2022.106942

Wen, X., Ma, S., Xu, X., & He, Y. (2008). Historical pattern and behavior of earthquake ruptures along the eastern boundary of the Sichuan-Yunnan faulted-block, southwestern China. *Physics of the Earth and Planetary Interiors*, *168*(1–2), 16–36. https://doi.org/10.1016/j.pepi.2008.04.013

Williams, A. J., Crossey, L. J., Karlstrom, K. E., Newell, D., Person, M., & Woolsey, E. (2013). Hydrogeochemistry of the Middle Rio Grande aquifer system—Fluid mixing and salinization of the Rio Grande due to fault inputs. *Chemical Geology*, *351*, 281–298. https://doi.org/10.1016/j.chemgeo.2013.05.029

Woith, H., Wang, R., Maiwald, U., Pekdeger, A., & Zschau, J. (2013). On the origin of geochemical anomalies in groundwaters induced by the Adana 1998 earthquake. *Chemical Geology*, *339*, 177–186. https://doi.org/10.1016/j.chemgeo.2012.10.012

Wu, T., Zhang, S., Li, M., Qin, W., & Zhang, C. (2016). Two crustal flowing channels and volcanic magma migration underneath the SE margin of the Tibetan Plateau as revealed by surface wave tomography. *Journal of Asian Earth Sciences*, *132*, 25–39. https://doi.org/10.1016/j.jseaes.2016.09.017

Wu, Z., Long, C., Fan, T., Zhou, C., Feng, H., Yang, Z., & Tong, Y. (2015). The arc rotational-shear active tectonic system on the southeastern margin of Tibetan Plateau and its dynamic characteristics and mechanism (in Chinese with English abstract). *Geological Bulletin of China*, *34*(1), 1–31.

Xiang, H., Guo, S., Xu, X., Zhang, W., & Dong, X. (2000). Active block division and present-day motion features of the south region of Sichuan-Yunnan Province (in Chinese with English abstract). *Seismology and Geology*, *22*(3), 253–264.

Xu, M., Wang, L., Liu, J., Zhong, K., Li, H., Hu, D., & Xu, Z. (2006). Crust and uppermost mantle structure of the Ailaoshan-Red River fault from receiver function analysis. *Science in China Series D: Earth Sciences*, *49*(10), 1043–1052. https://doi.org/10.1007/s11430-006-1043-8

Xu, S., Guan, L., Zhang, M., Zhong, J., Liu, W., Xie, X. g., et al. (2022). Degassing of deep-sourced CO_2 from Xianshuihe-Anninghe fault zones in the eastern Tibetan Plateau. *Science China Earth Sciences*, *65*(1), 139–155. https://doi.org/10.1007/s11430-021-9810-x

Xu, Y., Yang, X., & Liu, J. (2013). Tomographic study of crustal velocity structures in the Yunnan region southwest China (in Chinese with English abstract). *Chinese Journal of Geophysics*, *56*(6), 1904–1914. https://doi.org/10.6038/cjg20130613

Geochemistry, Geophysics, Geosystems 10.1029/2023GC011431

Xu, Z., Wang, Q., Li, Z., Li, H., Cai, Z., Liang, F., et al. (2016). Indo-Asian collision: Tectonic transition from compression to strike slip (in Chinese with English abstract). *Acta Geologica Sinica*, *90*(1), 1–23.

Yang, Y., Hu, S., Yao, H., Fang, L., & Wu, J. (2020). Crustal shear wave velocity and radial anisotropy in the Xiaojiang fault zone system (SE Tibet) revealed by ambient noise interferometry. *Tectonophysics*, *792*, 228594. https://doi.org/10.1016/j.tecto.2020.228594

Yasin, D., & Yüce, G. (2023). Isotope and hydrochemical characteristics of thermal waters along the active fault zone (Erzin-Hatay/Turkey) and their geothermal potential. *Turkish Journal of Earth Sciences*, *32*(6), 721–739. https://doi.org/10.55730/1300-0985.1871

Ye, T., Chen, X., Liu, Z., Wang, P., Dong, Z., Cui, T., et al. (2022). A magnetotelluric study of 3D electrical resistivity structure underneath the southern segment of the Red River fault zone, South China. *Journal of Asian Earth Sciences*, *225*, 105056. https://doi.org/10.1016/j.jseaes.2021.105056

Yin, A., & Harrison, T. M. (2000). Geologic evolution of the Himalayan-Tibetan orogen. *Annual Review of Earth and Planetary Sciences*, *28*(1), 211–280. https://doi.org/10.1146/annurev.earth.28.1.211

Yokoyama, T., Nakai, S. I., & Wakita, H. (1999). Helium and carbon isotopic compositions of hot spring gases in the Tibetan Plateau. *Journal of Volcanology and Geothermal Research*, *88*(1–2), 99–107. https://doi.org/10.1016/s0377-0273(98)00108-5

Yu, N., Unsworth, M., Wang, X., Li, D., Wang, E., Li, R., et al. (2020). New insights into crustal and mantle flow beneath the Red River fault zone and adjacent areas on the southern margin of the Tibetan Plateau revealed by a 3-D magnetotelluric study. *Journal of Geophysical Research: Solid Earth*, *125*(10), 105308. https://doi.org/10.1029/2020jb019396

Yuce, G., Fu, C. C., D'Alessandro, W., Gulbay, A. H., Lai, C. W., Bellomo, S., et al. (2017). Geochemical characteristics of soil radon and carbon dioxide within the Dead Sea Fault and Karasu Fault in the Amik Basin (Hatay), Turkey. *Chemical Geology*, *469*, 129–146. https://doi.org/10.1016/j.chemgeo.2017.01.003

Zhang, L., Guo, L., Zhou, X., Yang, Y., Shi, D., & Liu, Y. (2021). Temporal variations in stable isotopes and synchronous earthquake-related changes in hot springs. *Journal of Hydrology*, *599*, 126316. https://doi.org/10.1016/j.jhydrol.2021.126316

Zhang, M., Guo, Z., Xu, S., Barry, P. H., Sano, Y., Zhang, L., et al. (2021). Linking deeply-sourced volatile emissions to plateau growth dynamics in southeastern Tibetan Plateau. *Nature Communications*, *12*(1), 4157. https://doi.org/10.1038/s41467-021-24415-y

Zhao, C., Wang, Y., Zhou, Z., Li, Z., & Xing, L. (2017). Present-day temperatures of magma chambers in the crust beneath Ninger volcanic field, southwestern China: Estimation from CO_2-CH_4 carbon isotope geothermometer (in Chinese with English abstract). *Acta Petrologica Sinica*, *33*(1), 231–249.

Zhao, K., Jiang, G., Yang, Y., Liu, D., Liu, Y., & Wang, L. (2005). Brief analysis of the reasons of CO_2 degassing from hot springs on main faults within the east of Yunnan (in Chinese with English abstract). *Earth and Environment*, *33*(2), 11–15.

Zheng, G., Wang, H., Wright, T. J., Lou, Y., Zhang, R., Zhang, W., et al. (2017). Crustal deformation in the India-Eurasia collision zone from 25 years of GPS measurements. *Journal of Geophysical Research: Solid Earth*, *122*(11), 9290–9312. https://doi.org/10.1002/2017jb014465

Zheng, T., Stefánsson, A., Kang, F., Shi, M., Jiang, H., & Sui, H. (2023). Geochemical and isotope constraints on the hydrogeology and geochemistry of the geothermal waters in the Shandong Peninsula, China. *Geothermics*, *108*, 102628. https://doi.org/10.1016/j.geothermics.2022.102628

Zhou, X., Wang, W., Li, L., Hou, J., Xing, L., Li, Z., et al. (2020). Geochemical features of hot spring gases in the Jinshajiang-Red River fault zone, Southeast Tibetan Plateau (in Chinese with English abstract). *Acta Petrologica Sinica*, *36*(7), 2197–2214. https://doi.org/10.18654/1000-0569/2020.07.18

Zhou, Y., Yue, H., Zhou, S., Fang, L., Zhou, Y., Xu, L., et al. (2022). Microseismicity along Xiaojiang Fault Zone (Southeastern Tibetan Plateau) and the characterization of interseismic fault behavior. *Tectonophysics*, *833*, 229364. https://doi.org/10.1016/j.tecto.2022.229364

References From the Supporting Information

Weiss, R. F. (1971). Solubility of helium and neon in water and seawater. *Journal of Chemical & Engineering Data*, *16*(2), 235–241. https://doi.org/10.1021/je60049a019